Facile synthesis of paratoluene sulfonic acid assisted S-doped polyaniline hybrid composite for energy storage devices

Tapas Das[1] and Bhawna Verma[1,*]

[1] Department of Chemical Engineering & Technology, IIT BHU, Varanasi 221005, India

ABSTRACT

Ternary composites were prepared by varying the weight ratio of the individuals, and their electrochemical performances were recorded by cyclic voltammetry, charging-discharging, and electrochemical impedance spectroscopy. Polyaniline-acetylene black-cobalt ferrite having the weight ratio of 4:1:2 (aniline:acetylene black:cobalt ferrite) gave outstanding electrochemical outputs. The corresponding system (4:1:2 ratio based system) had 294.49 F/g of specific capacitance at 1 mA of current for the two-electrode configuration. It exhibited the maximum coulombic efficiency of 99.1%. Specific energy and power values are the highest for this system, which are 40.9 Wh/kg and 125 W/kg, respectively. It has quite good capacitance retention of 83.5% after 8000 cycles. The charge transfer resistance is only 1 Ω for this system.

1 Introduction

Increasing demand for energy and fall in fossil fuel reserves have forced the researchers to focus on the making of excellent energy storage devices. The existing storage devices are fuel cells, batteries, conventional capacitors, supercapacitors, etc. Batteries and fuel cells have higher energy density but possess lower power density, high cost, less safety, difficulty in fabrication, and less cycle life. Conventional capacitors have a long life span and high power density, but it has a low energy density compared to fuel cells and batteries. Therefore, supercapacitors have emerged in the world of energy and storage devices, which fill the space between batteries and conventional capacitors with its high energy and power density, low cost, outstanding life span, safety, and eco-friendliness [1–3].

On the basis of charge storage on the surface and electrode materials, supercapacitors are of three types, i.e., hybrid supercapacitor, pseudocapacitor (PC), and electric double-layer capacitor (EDLC). In EDLC, the ionic and electronic charges are separated at the electrolyte and electrode interface. Pseudocapacitors work on the basis of surface redox reactions and reactions at the active sites of the materials. Hybrid supercapacitors store charge by both double layer formation and redox reactions [4, 5]. Carbon materials such as graphene, carbon nanotube,

Address correspondence to E-mail: bverma.che@itbhu.ac.in

acetylene black, activated carbon, etc. show EDLC behavior. Metal oxides such as RuO_2 [6], MnO_2 [7], CuO [8], and conducting polymers (CPs) such as polyaniline, polypyrrole, polythiophene [9], etc. are pseudocapacitive in nature. Out of all the conducting polymers, polyaniline is found to have more conducting nature when it is doped with an acid [10, 11]. Paratoluene sulfonic acid (PTSA), Camphor sulfonic acid (CSA), oxalic acid, etc. are various organic acids, which are used as doping agent during polyaniline synthesis as they make polyaniline hydrophilic and enhance its electrochemical properties. Use of these organic acids create conjugation in the polyaniline chain due to protonation and increase the electrical activity [12, 13]. Individual material has some drawbacks like less cycle life (pseudocapacitive materials) and low energy density (carbon-based materials). Various binary composites based on CP/carbon, CP/metal oxide, metal oxide/carbon have been formed by many researchers to counter the specific disadvantages. Still, the binary composites demonstrate an inferior energy density than batteries. Therefore, researchers opted to develop ternary composites of conducting polymer, carbon material, and metal oxides. These ternary composites exhibited outstanding energy density without any loss in power density, high-specific capacitance, low diffusive resistance, low internal resistance, high active surface area, and enhanced cycle life [14–16].

Bin et al. reported 395 F/g of specific capacitance at 10 mA/cm² with 92% capacitance retention after 1000 cycles for graphene, polyaniline, and MnO_2 ternary electrode [17]. Kalimuthu et al. synthesized $MnFe_2O_4$-graphene-polyaniline-based system having 241 F/g capacitance at 0.5 mA/cm² [18]. Amit et al. developed polyaniline-MoO_3-graphene-based ternary composite, which had 593 F/g of capacitance at 1 A/g along with 92.4% retention over 1000 cycles [19]. Luyan et al. fabricated a ternary electrode system (graphene-Au-polyaniline), which exhibited a specific capacitance of 572 F/g at 0.1 A/g [20]. Chao et al. reported a ternary electrode system consisting of polyaniline-MnO_2-graphene, which showed 875.2 F/g of specific capacitance at 0.2 A/g [21]. Anukul et al. obtained 350 F/g of capacitance at 1 A/g for polyaniline-carbon nanotube-MoS_2 ternary electrode [22]. Aadithya et al. worked on polyaniline-rGO-CeO_2-based ternary system and reported a capacitance of 684 F/g and 92% retention after 6000 cycles [23]. Jiayi et al. synthesized a composite of polyaniline-manganese dioxide-carbon nanofiber and tested the electrochemical properties by three-electrode configurations. 587.3 F/g of capacitance was obtained at 0.5 A/g and the electrode retained 84% of the initial capacitance after 1000 cycles [24]. Prasenjit et al. reported a capacitance value of 476 F/g at a current density of 2 A/g for Co_3O_4-polyaniline-graphene-based electrode [25]. In the above-mentioned researches, the authors have reported better electrochemical properties of the ternary composites in compared to the individual materials.

In our previous research, we have reported that the ternary polyaniline/acetylene black/cobalt ferrite system has superior electrochemical performance than the individual systems [26]. The current research has been performed to find out the optimized proportion (weight ratio) of the individual components on the basis of their specific capacitance, energy density, power density, and cycle life. There is no report on the optimization of weight ratio of the polyaniline-acetylene black-cobalt ferrite system.

2 Materials and methods

2.1 Materials used

Nitrates precursors of cobalt and iron, glycine, ammonium persulfate (APS), Paratoluene sulfonic acid (PTSA) were taken from SRL India. Acetylene black (AB), aniline (AN) monomer, Nafion solution had been brought from Alfa aesar.

2.2 Synthesis of composites

Ternary composite of polyaniline-acetylene black-cobalt ferrite was synthesized by chemical oxidative polymerization (COP) reaction of aniline along with subsequent addition of acetylene black and cobalt ferrite. In the COP technique, aniline was added dropwise to the PTSA solution followed by dropwise and very slow addition of APS to initiate the polymerization process keeping the temperature constant between 0 and 4 °C under continuous stirring. During the ongoing process of polymerization, desired amount of AB and COF were added to the solution as per Table 1. After complete addition of APS, the mixture turned into dark green color from brown, which was the indication of the formation of conducting polyaniline. Then the solution was kept in

the refrigerator, vacuum filtered after 12 h and dried with the help of a vacuum oven at 60 °C.

2.3 Electrode fabrication

Slurries of the active materials were prepared by mixing ternary composites (5 mg) with 2-propanol (0.2 mL), and nafion (12 μL). Electrodes for the supercapacitors were fabricated by dropcasting the composite slurry on the carbon paper substrate, which was connected to the copper wire current collector. Figure 1 contains the photographs of fabricated electrode and device. In case of three electrode system, working electrode, reference and counter electrode are connected separately to their corresponding leads. In case of two electrode system, working electrode is connected to one terminal of the device and the other terminal of the device is connected to the reference and counter electrode.

2.4 Material characterization

Crystalline natures of the synthesized materials were examined by Rigaku miniflex 600 desktop X-ray diffraction (XRD) system at 5°/min between 2θ = 10 and 80° keeping λ = 0.154 nm. Nicolet iS5-Thermo electron scientific instruments LLC was used to run Fourier transform infrared spectroscopy (FTIR) and recognize the functional groups existing in the material. Nova Nano SEM 450 (FEI company of USA (SEA) PTE, LTD) was used to perform microstructural analysis of PACOF1 by FESEM technique. Elemental percentages of the constituents were estimated by EDS analysis performed by "Team Pegasus Integrated EDS-EBSD with octane plus and Hikari Pro equipped with the SEM machine". Thermal analyser, STA 8000 and 8500 Perkin Elmer Ltd. Was used to perform thermogravimetric analysis

(TGA) in a temperature range of 30 to 800 °C at 10 °C/min (inert atmosphere created by N_2 gas). Specific surface area (SSA) of the prepared samples were analysed by Brunauer–Emmette–Teller (S_{BET}) after getting the required absorption–desorption data from the surface analyzer (MICROMERITICS-ASAP 2020). The X-ray photoelectron spectroscopy (XPS) was carried out by X-ray photoelectron spectrometer (AMICUS, Kratos Analytical). The micrograph of PACOF1 was captured by high-resolution transmission electron microscope (HR-TEM) (Tecnai G2 20 TWIN, FEI company of USA (SEA) PTE, LTD) to obtain morphology of the synthesized composite. Phase identification of the components in the composite was accomplished by the selected area diffraction (SAED) pattern.

2.5 Electrochemical characterizations

Electrochemical measurements of the fabricated electrodes and symmetric (cells) supercapacitors were done by Versastat 3. Cyclic voltammetry (CV) measurements had been done at 5 mV/s within a stable potential of − 0.2 to 0.8 V. charging–discharging (CD) measurements had been performed at 1 mA of current. Platinum was used as reference electrode, Ag/AgCl as counter electrode, and the prepared material as working electrode in three-electrode configurations. 2 mg of synthesized material was loaded in three-electrode configuration. Two electrode cell configuration was consisting of two exactly same electrodes (each electrode was loaded with 2 mg active material). 10 mV of AC amplitude was applied over 100 kHz to 0.01 Hz frequency in the electrochemical system to find out impedance of the system, and this technique is known as electrochemical impedance spectroscopy (EIS). 1 M KOH solution was taken as the electrolyte to perform the electrochemical testing.

3 Results and discussions

3.1 XRD

X-ray diffraction (XRD) patterns of all the composites have been given in Fig. 2. Pristine polyaniline (PA or PANI) had diffraction peaks at 14.77°, 20.72°, 24.93° (see Fig. S1). The characteristic peaks of acetylene black (AB) were seen at 26.09° and 43.33° (Fig. S1). In
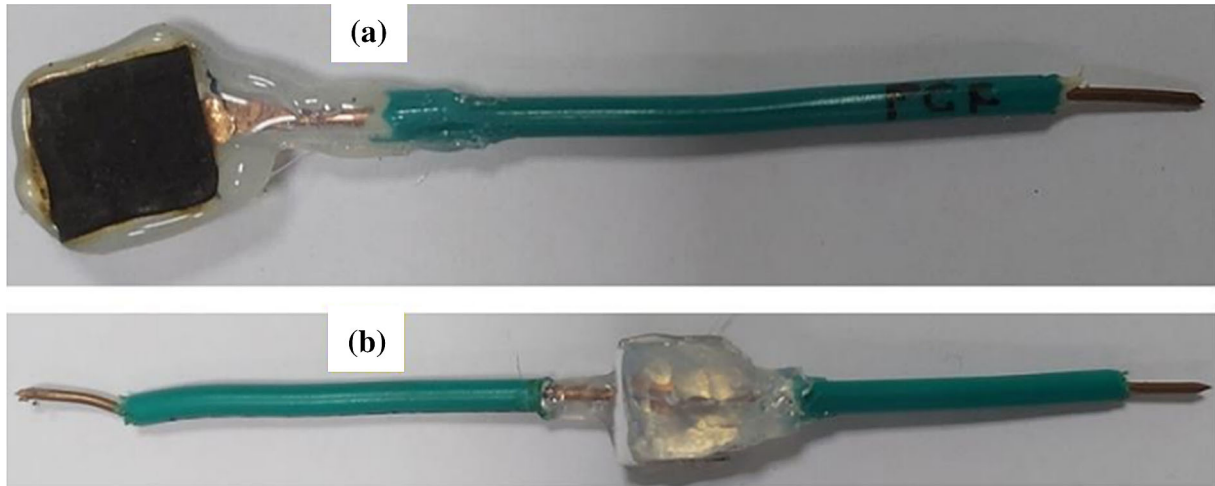
Table 1 Ternary composites and the corresponding weight ratio of the individual components

Material	Weight ratio (AN:AB:COF)
PACOF1	4:1:2
PACOF2	4:1:3
PACOF3	4:2:1
PACOF4	4:3:1
PACOF5	4:1:1
PACOF6	4:1:4
PACOF7	4:4:1

Fig. 1 Fabricated **a** electrode and **b** assembled two electrode (device)

the composites, the polyaniline peaks at 20.72°, 24.93° had been shifted to 21.15° and 23.47°, respectively. In case of acetylene black, the peak at 26.09° was shifted to 25.37°. XRD characteristic peak of cobalt ferrite (COF) exists at 35.47°. 2-theta values of all the diffraction peaks of COF are 18.32° (111), 30.12° (220), 35.49° (311), 37.13° (222), 43.15° (400), 53.48° (422), 57.04° (511), 62.59° (440), 74.10° (533). These peak values reflect that all three components have been successfully incorporated in the ternary composites. Peak intensities of PA and AB decrease with a higher amount of COF as their mass-volume proportion decrease [27].

3.2 FTIR

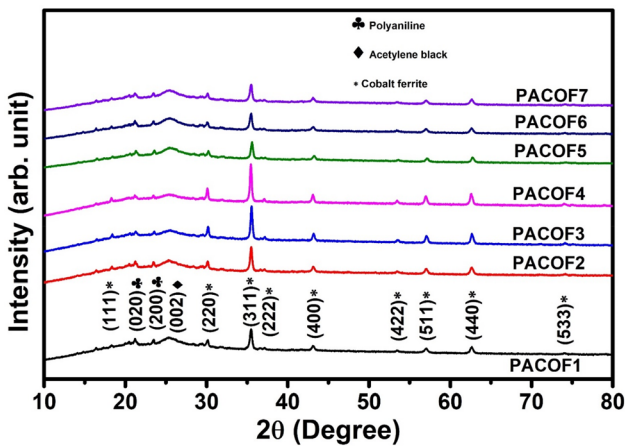Fourier transform infrared spectroscopy (FTIR) of all the synthesized ternary composites have been given in Fig. 3. Functional groups and their corresponding peak positions have been provided in Table 2. Spectroscopic peaks at 567 cm^{-1} and 676 cm^{-1} could be due to Fe–O and Co–O functional groups present in cobalt ferrite [1, 28]. S–O stretching or –CH deformation could have resulted in the spectrum at 795 cm^{-1} [17, 29]. Symmetric and asymmetric stretching vibration of O=S=O group residing in the dopant (PTSA) could be the reason behind the spectroscopic peak at 1006 cm^{-1} [30]. The spectrum at wave number 1114 cm^{-1} could be due to the stretching vibration of –N=Q=N– group [31]. Another probable reason could be the C–H plane bending vibration, which occurred during protonation. The
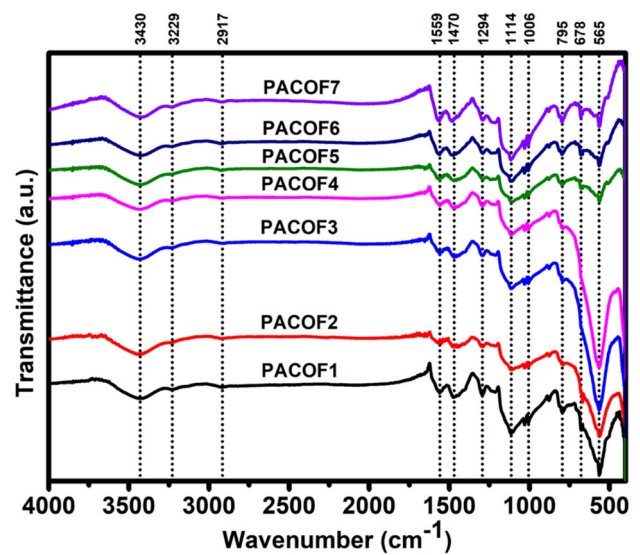

Fig. 2 XRD of all the prepared composites

Fig. 3 IR spectroscopies of all the prepared samples

Table 2 Wavenumbers and corresponding functional groups

Wavenumbers (cm^{-1})	Functional groups
565	Fe–O
678	Co–O
795	–CH/S–O
1006	O=S=O
1114	–N=Q=N–
1294	C–N
1470	C=C
1559	C=C
2917	NH
3229	–OH
3430	–CH/NH_2^+

spectroscopic band at 1294 cm^{-1} could be the stretching of C–N and C–N^+, which is associated with the protonation during polymerization of polyaniline [32]. Benzenoid and quinoid ring have spectroscopic bands at 1470 cm^{-1}, and 1559 cm^{-1}, respectively, and they are associated with the stretching vibrations of C=C [33, 34]. FTIR peaks at 2917 cm^{-1} and 3430 cm^{-1} are the stretching modes of NH and NH_2^+ existing in polyaniline [34, 35]. Band at 3229 cm^{-1} could be referred to stretching vibration of –OH group [36].

3.3 FESEM

High resolution field emission scanning electron microscopy (FESEM) image of PACOF1 was taken to study the microstructural surface behavior (Fig. 4). FESEM micrograph of only PACOF1 has been given because all the composites have mostly same morphology as they all have the same components (polyaniline, acetylene black, and cobalt ferrite) with different ratio. Rod-like texture and interconnected network structures are found for PACOF1. The interconnected web-like structure could be due to the crosslinking during polymerization, and rod-like texture could be due to polyaniline [37]. The upper surface is mostly covered by polyaniline, which is creating a conductive layer (as PA is a conducting polymer). Rod shapes of polyaniline can be justified by the theory of micelle formation. PTSA is amphophilic in nature and helps in structural reformation due to –SO_3H hydrophilic group and C_7H_8 lipophilic chain in it. A soft template of aniline-PTSA complex would have formed when –NH_2 of aniline and –
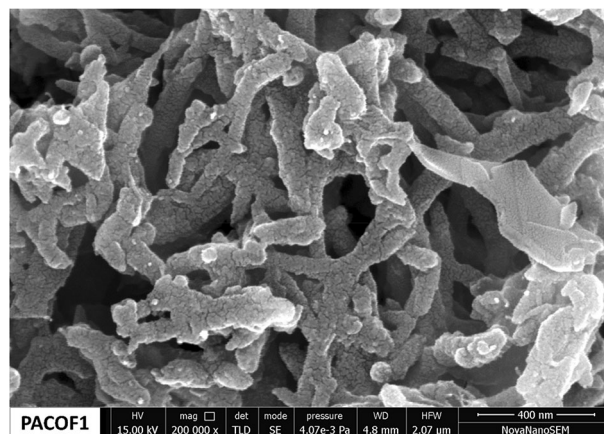
Fig. 4 FESEM image of PACOF1

SO_3H of PTSA reacted with each other after adding aniline to PTSA solution. Then the soft template would have acquired rod-shaped texture after adding APS to aniline-PTSA solution to commence polymerization of aniline.

3.4 EDX

EDX analysis has been done to find out the elemental distribution of individual components over the surface of the composite material. The spectrum and table attached to it in Fig. 5 demonstrate the elemental atomic and weight percentages. The obtained atomic ratio of Co and Fe is approximately 1:2, which shows homogeneousness in the distribution of the individual components over the surface of the prepared composite.

3.5 TGA

Figure 6 demonstrates the thermogravimetric analysis of the synthesized hybrid systems. A visible weight loss was observed at about 110 °C. Till 300 °C, the weight lost at a slower rate which could be because of the elimination of water from the hybrid samples. After 200 °C, the conducting networks of polyaniline starts to lose the intactness and a weight loss is observed. The maximum weight was lost between 300 to 500 °C which could be assigned to the combustion of polyaniline and acetylene black [38]. TG curves were almost stable after 610 °C as all the portions of acetylene black and polyaniline were removed. Finally, the weight percentages of metal components were left over (see Table S3). The weight
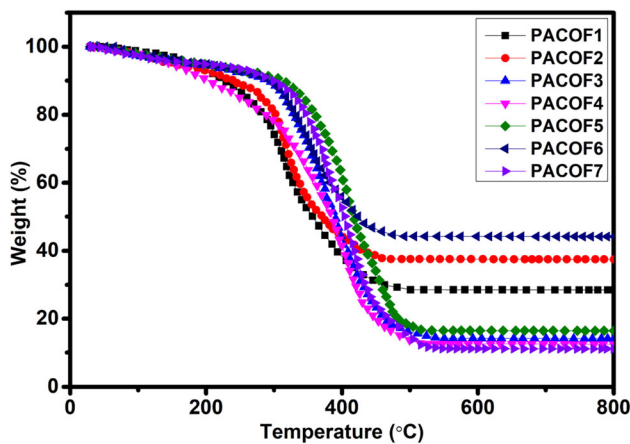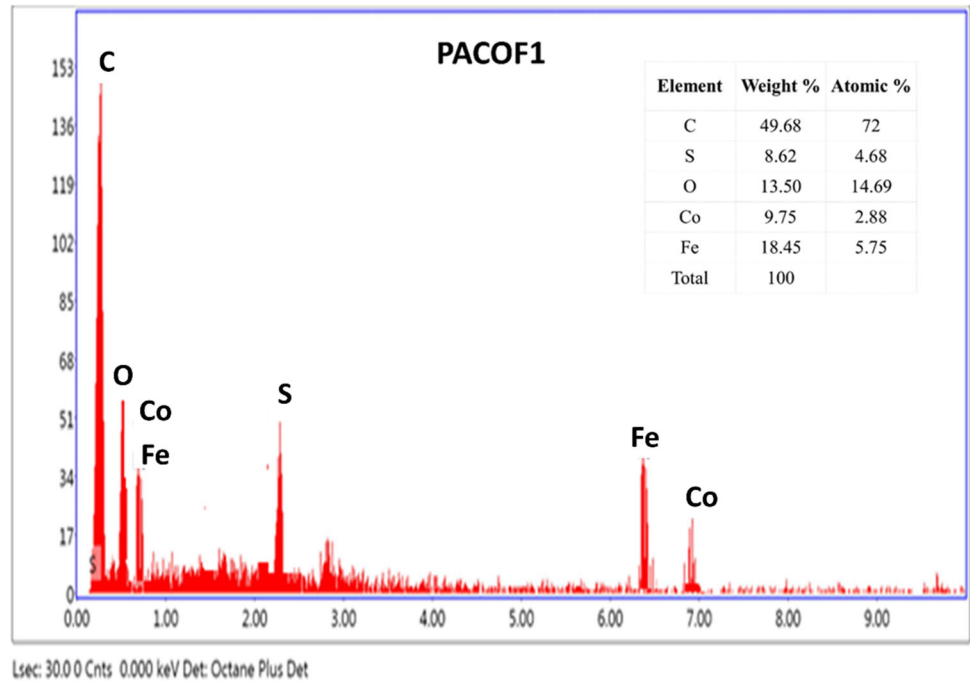
Fig. 5 EDX of PACOF1

Fig. 6 TGA of the prepared composite materials

percentages of cobalt ferrite were decreasing gradually with the increase in acetylene black (TGA curve).

3.6 BET

The BET technique was followed to estimate specific surface area (SSA) of the prepared composites and find out its correlation with charge storage ability. Figure 7 represents the adsorption–desorption isotherms of the corresponding composite materials. SSAs estimated from BET have been provided in Table S3. The highest SSA of 302 m²/g was obtained for PACOF7 which could probably be due to the existence of minimum amount of cobalt ferrite and

maximum amount of acetylene black and polyaniline. In our previous study we found that AB, PA, and COF had SSAs of 223 m²/g, 112 m²/g, and 16 m²/g, respectively [26]. PACOF6 (4:1:4) had the least SSA of 93 m²/g. The primary cause could be the existence of more amount of COF particles, which might be blocking the active pores of AB and PA. When aniline:AB:COF was 4:1:1, the SSA was 202 m²/g and obtained specific capacitance was 620.27 F/g. For the ratio 4:1:2, the calculated specific capacitance and SSA were 738.65 F/g and 196 m²/g, respectively. For the ratio 4:1:3, the SSA was 147 m²/g but the specific capacitance was greater than the
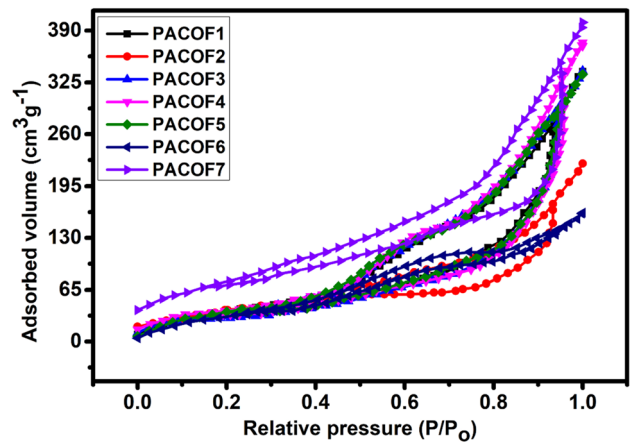
Fig. 7 BET of the prepared composite materials

specific capacitance obtained for the ratio 4:1:1, i.e. 701.89 F/g. The above results concludes that there is no specific relation between specific capacitance and specific surface area. So, SSA can not be claimed as a deciding factor for charge storage ability.

3.7 XPS

In XPS, the oxidation states of all the elements are predicted based on the binding energies they posses (Fig. 8). C1s had three deconvoluted peaks positioned at 284.6, 285.4, and 287.2 eV, and these can be attributed to benzene ring (C–C/C–H), C–N/C=N and quinoid ring (C=O), respectively [39]. O1s spectrum had three peaks at 529.8, 531.6, and 533.5 eV, and they could be ascribed to the bonding between metal–oxygen, surface oxygen, and hydroxyl group, respectively [40]. N1s exhibited peaks at 398.6, 400.2, and 401.5 eV. The spectrum at 400.2 eV and 398.6 eV were attributed to pyrrolic-N and pyridinic-N, respectively. The deconvoluted spectrum at 401.5 eV could be due to the interaction between N^+ ion and protons of PTSA [41]. Spectrum of Co 2p was fitted in four different peak positions of 780.6 eV, 785.4 eV, 796.1 eV, and 802.8 eV. 780.6 eV and 785.4 eV could be assigned to $Co2p_{3/2}$ and $Co2p_{3/2}$ satellite peak, respectively. $Co2p_{1/2}$ and $Co2p_{1/2}$ satellite spectrum were located at 796.1 eV and 802.8 eV, respectively. Iron has four deconvoluted peaks positioned at 711.1 eV, 714.3 eV, 724.6 eV, and 733 eV. 711.1 eV and 714.3 eV could be ascribed to $Fe^{3+}2p_{3/2}$ and its satellite peak. Peaks positioned at 724.6 eV and 733 eV could be assigned to $Fe^{3+}2p_{1/2}$ and its satellite peak [42, 43].
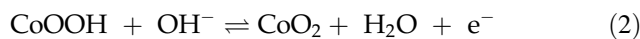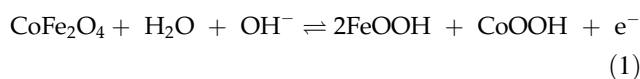
3.8 TEM

The TEM micrographs of PACOF1 have been exhibited in Fig. 9. We can observe mixture of large and small particles from the bright filed image, which is due to the coexistence of three materials (acetylene black, cobalt ferrite, and polyaniline) in the composite. The large particles are due to the presence of cobalt ferrite and small particles are because of PANI and AB. From the SAED pattern, it can be clearly seen that the composite shows polycrystalline nature. The clear and concentric rings are because of the crystalline nature of cobalt ferrite. The diffused rings are due to the amorphous nature of acetylene black. The obtained d-spacing values are 2.89, 2.48, 1.98, 1.68,

1.41 Å which represent (220), (311), (400), (422), (440) planes of cobalt ferrite.

3.9 Electrochemical analysis

To find out the electrocatalytic behavior and various redox transitions of the constituents in the composite, cyclic voltammetry (CV) was conducted at 5 mV/s, and the recorded graphs are given in Fig. 10a–d. Polyaniline and cobalt ferrite exhibit pseudocapacitive nature and undergo redox process, where as acetylene black shows EDLC behavior. Polyaniline showed redox behavior at potentials of 0.28 V/0.04 V, 0.56 V/0.41 V, 0.72 V/0.63 V and oxidation occurred at 0.25 V and 0.62 V for cobalt ferrite (Fig. S2) [26]. In our earlier research, pristine polyaniline had an oxidation peak at 0.56 V in CV plot, which was because of a degraded by-product, i.e., benzoquinone/hydroquinone [34]. The fading of peak at 0.56 V in all the ternary composites spectacles that the development of benzoquinone/hydroquinone has been ceased by the insertion of AB and COF. At 0.28 V and 0.72 V, leucoemeraldine changes to emeraldine salt and emeraldine salt gets converted to pernigraniline, respectively (see schematic diagram given in Fig. 11).

$$CoFe_2O_4 + H_2O + OH^- \rightleftharpoons 2FeOOH + CoOOH + e^- \quad (1)$$

$$CoOOH + OH^- \rightleftharpoons CoO_2 + H_2O + e^- \quad (2)$$

$$FeOOH + H_2O \rightleftharpoons Fe(OH)_3 \leftrightarrow (FeO_4)^{2-} + 3e^- \quad (3)$$

Equation 4 and 5 are applied to evaluate specific capacitances in two and three-electrode configurations.

$$CSC,2E = \frac{\int I * dV}{MT * v * \Delta V} \quad (4)$$

$$CSC,3E = \frac{\int I * dV}{M * v * \Delta V} \quad (5)$$

$CSC,3E$ and $CSC,2E$ are the specific capacitances (F/g) of three and two electrode systems, respectively. $\int I * dV$ is the area under cathodic scan, M is the mass of single electrode (mg), MT is the total mass of active material in the cell, v refers to the scan rate (in mV/s), and ΔV signifies stable potential range (in V).

The specific capacitance values from CV have been provided in Table 3.

Cyclic voltammetry (CV) curve area under PACOF1 based system is larger than other systems,
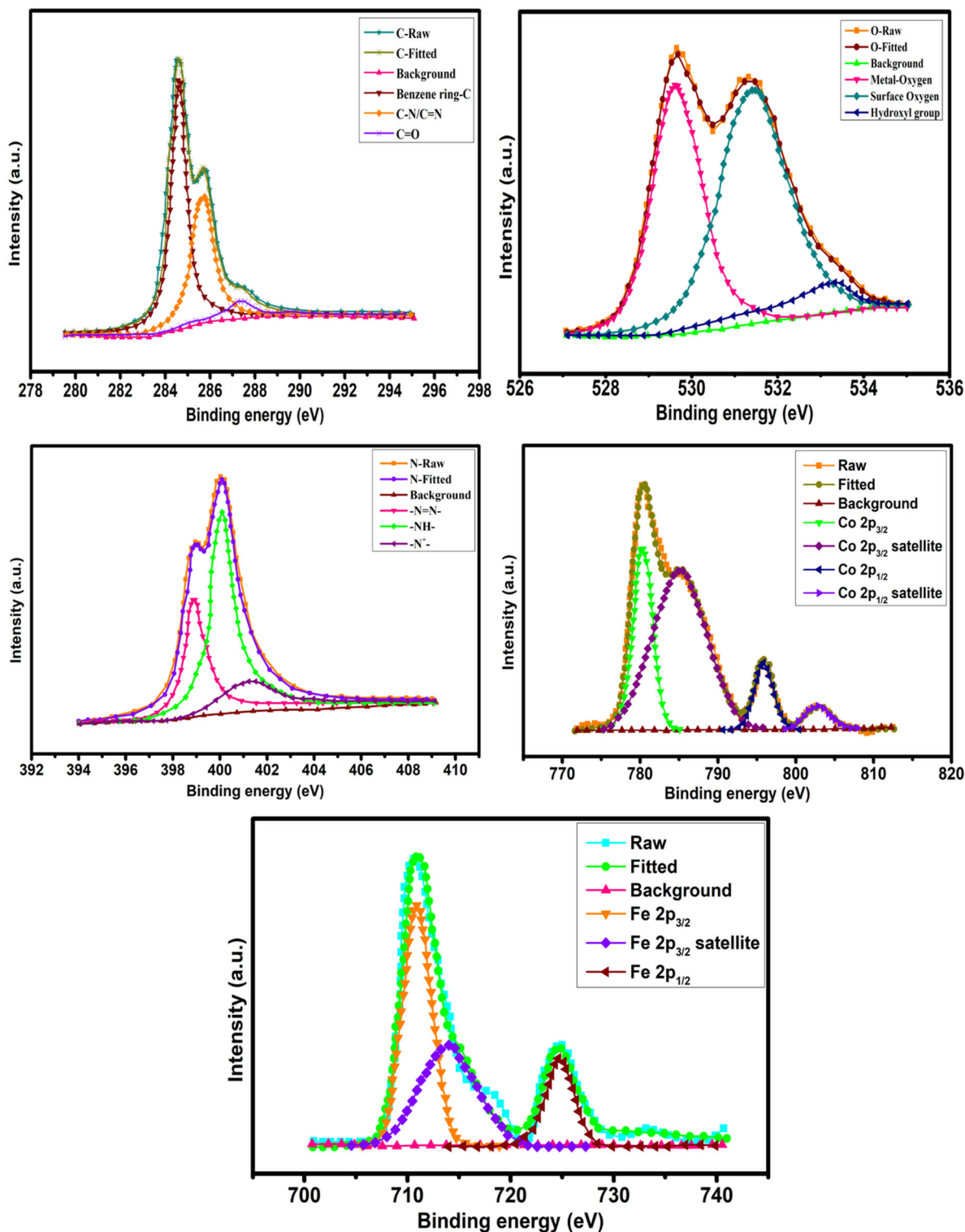
Fig. 8 XPS of PACOF1 composite

and it also demonstrates the highest current in the CV curve (Fig. 10a,c). This evidences its exceptional electrochemical performance, electron mobility, and ionic conductivity [44]. Two and three-electrode system of PACOF1 displays the highest specific capacitances of 288.93 F/g and 738.65 F/g,
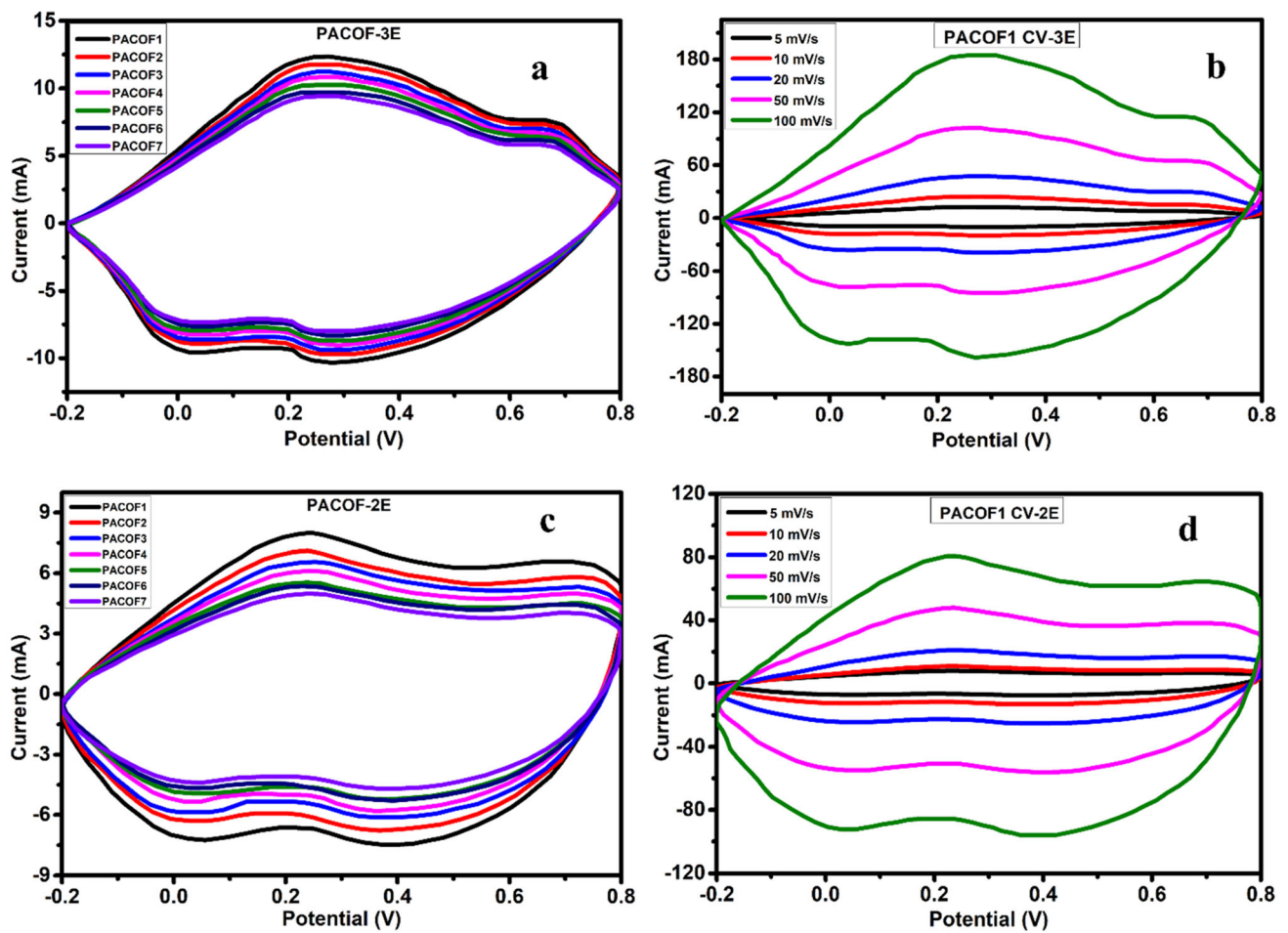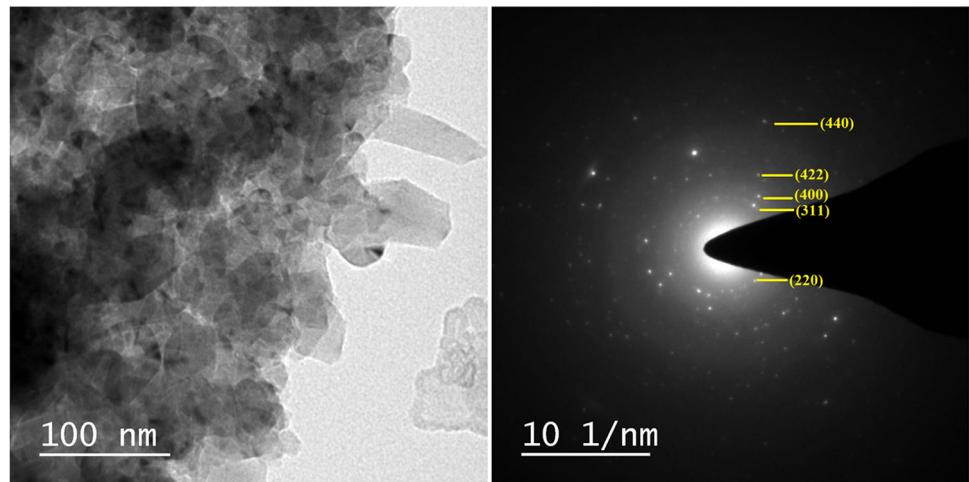
Fig. 9 TEM of PACOF1
composite

Fig. 10 **a**, **c** CV of all the systems in KOH electrolyte for three-electrode and two electrode configuration at 5 mV/s. **b**, **d** CV of PACOF1 for three and two electrode systems at different scan rates

respectively. So, 4:1:2 (AN:AB:COF) can be considered to be the optimal proportion on the basis of its current response and charge holding ability. The

electrochemical behavior of PACOF1 was observed at various scan rates. It is found that the peak current increases with the scan rate. In the mean while, from

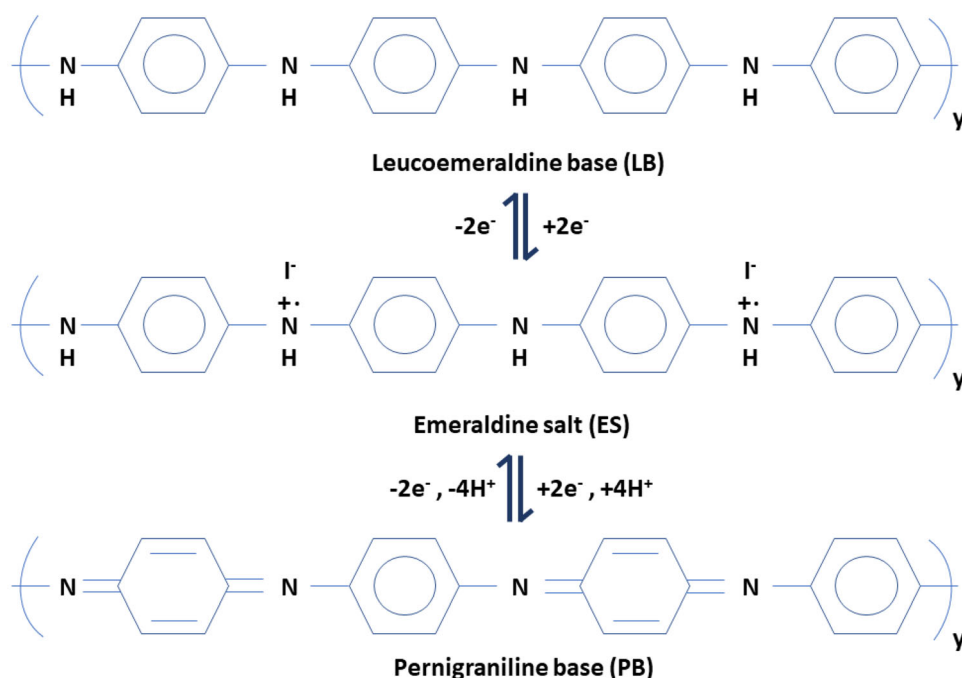**Fig. 11** Schematic of redox conversions of polyaniline

Leucoemeraldine base (LB)

$-2e^-$ $+2e^-$

Emeraldine salt (ES)

$-2e^-, -4H^+$ $+2e^-, +4H^+$

Pernigraniline base (PB)

Table 3 Specific capacitances obtained from different configurations

| Material	Weight ratio (AN:AB:COF)	$CV_{SC,3E}$ (F/g)	$CV_{SC,2E}$ (F/g)	$CD_{SC,2E}$ (F/g)	Specific power (W/kg)	Specific energy (Wh/kg)	Coulombic efficiency, η (%)
PACOF1	4:1:2	738.65	288.93	294.49	125	40.9	99.1
PACOF2	4:1:3	701.89	258.53	275.57	125	38.27	98.6
PACOF3	4:2:1	673.47	238.25	257.56	125	35.77	98
PACOF4	4:3:1	644.46	219.63	253.06	125	35.14	97.4
PACOF5	4:1:1	620.27	201.66	247.65	125	34.39	96.7
PACOF6	4:1:4	592.88	196.55	223.34	125	31.01	95.5
PACOF7	4:4:1	568.22	179.91	206.23	125	28.64	94.3

Fig. 12 it can be seen that the specific capacitance is decreasing with the increase in potential scan rate (Table S4). FESEM image illustrates that the uppermost surface is covered by rod-shaped polyaniline, and this could be offering ample conducting networks for the movement of charges [45]. The available voids must be giving ample path for ion/electron transport, resulting in rapid electrochemical activities. Use of a larger amount of metal oxide (COF) or carbon (AB) gives rise to pore blockages, which in turn hinder the ion and electron transfer within the porous channel of fabricated systems [46, 47]. Integration of both EDLC (AB) and pseudocapacitive (PA and COF) systems in a single composite lead to excellent electrochemical activity by overcoming numerous limitations of the individual constituents. Acetylene black contributes to the specific capacitance through physical adsorption of the charges, where as polyaniline and cobalt ferrite contribute through their redox transitions. So, it's necessary to uncover the appropriate proportion at which the ions and electrons will experience a smooth passage, which will bring superior electrochemical properties.

The shapes of CD plots are nearly symmetric for all the cells and are mostly linear in nature. This infers that the systems have negligible IR drop. The slight deviations of the CD plots could be due to the redox transitions of the redox active materials like polyaniline and cobalt ferrite.

Details of the Charge–discharge (CD) behavior of the assembled supercapacitors (two-electrode

Fig. 12 Scan rate vs specific capacitance plot of PACOF1
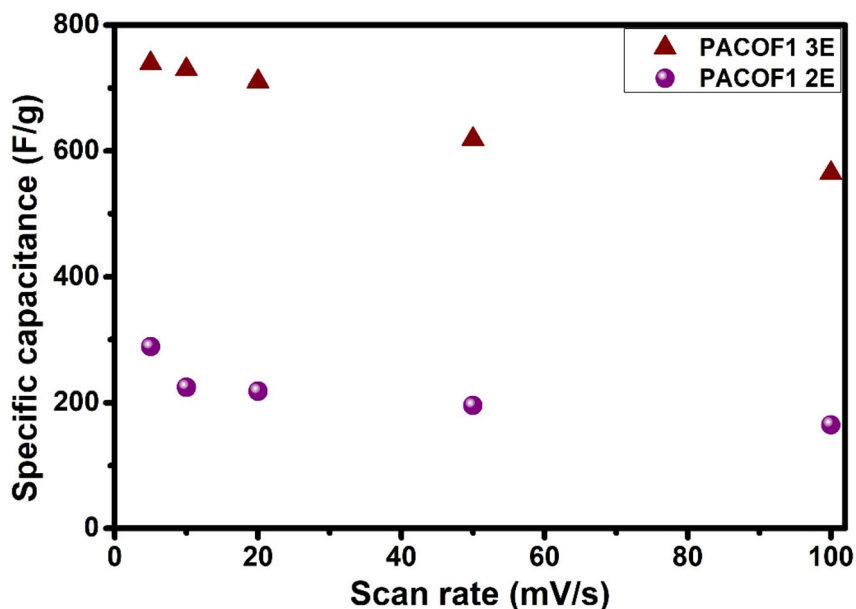
systems) were acquired at 1 mA of current and for PACOF1 we checked the charging-discharging profile at different current. Figure 13a shows the CD patterns of PACOF based two electrode systems, and PACOF1 has the largest discharging time in compared to all other composites. With the increase in current, the charging and discharging time of PACOF1 is decreasing (Fig. 13b). The calculated specific capacitance is also decreasing with increase in current (Fig. 14). All the systems have a negligible IR drop during CD process. The curves present nearly symmetric and linear patterns, suggesting better reversibility. This could be due to the fast movement of electrons and electrolyte ions in the conductive channels and preferably the higher charge storage ability of the systems.

Equation 6 is applied to calculate specific capacitances from the CD plot.

$$CSC,2E = \frac{I * TD}{MT * \Delta V} \tag{6}$$

where I and T_D are the discharging current (mA) and discharging time (s), respectively.

All the calculated specific capacitance (C_{SP}) values have been given in Table 3, and PACOF1 has the highest C_{SP} of 294.49 F/g. So, the CD analysis also proposes that 4:1:2 (AN:AB:COF) is the optimal proportion on the basis of charging and discharging efficiency of the fabricated cells. It is worth
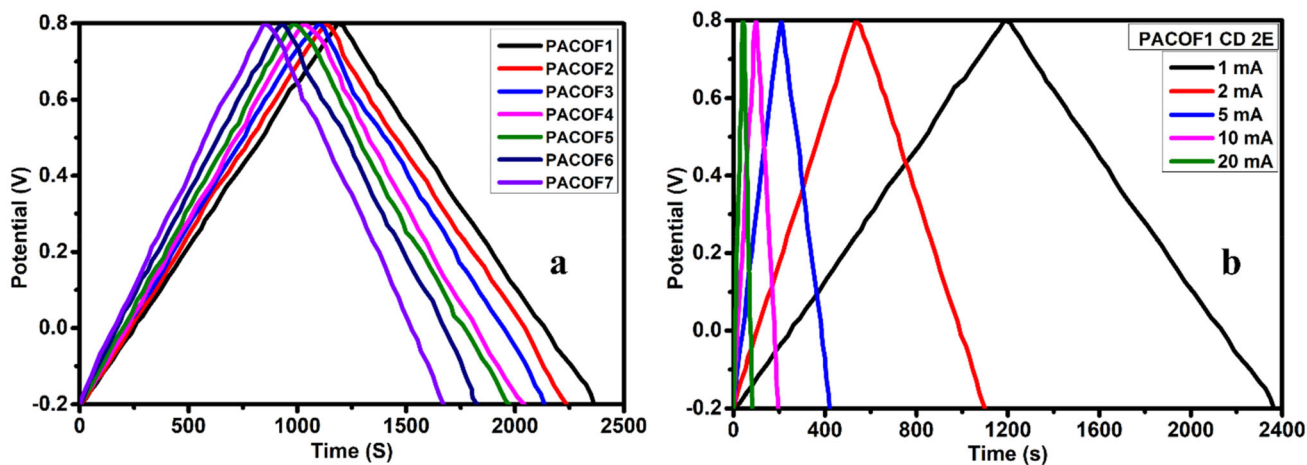

Fig. 13 **a** CD of all the systems for two electrode configuration at 1 mA, **b** CD of PACOF1 for two electrode systems at different current
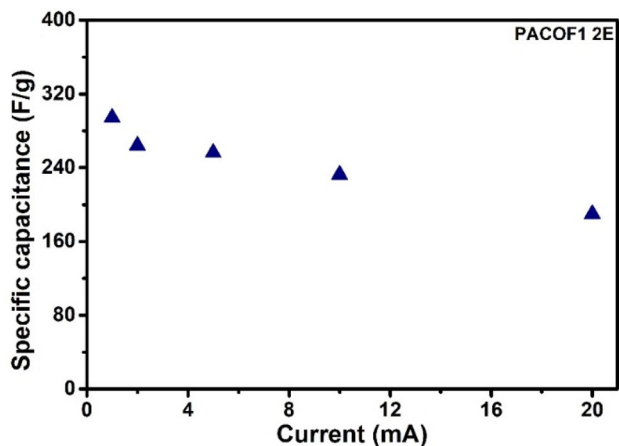
Fig. 14 Current vs specific capacitance plot for PACOF1

mentioning that the C_{SP} is the lowest for the ratio 4:4:1, i.e., 206.23 F/g. With the addition of more AB, PA, and COF particles would have been scattered abruptly over the surface of AB, creating a discontinuous conducting network [48]. Similarly, the inclusion of more COF particles would have created micro-sized COF particles as a result of aggregation. The aggregated COF particles would have obstructed the electron and ion mobility into the electroactive centers and bulk of the fabricated electrodes [49, 50].

The potential to hold charge and ability to deliver to a system is estimated from the specific energy and power of the cells. Equations used to calculate specific energy and power are given below.

$$E_{SE} = \frac{1}{2} C_{SC,2E} V^2 \qquad (7)$$

$$P_{SP} = \frac{E_{SE}}{T_D} \qquad (8)$$

where, E_{SE} = Specific energy (Wh/kg), P_{SP} = Specific power (W/kg).

E_{SE} and P_{SP} values are found to be the highest for PACOF1, i.e., 40.9 Wh/kg and 125 W/kg, respectively (Fig. 15). The exceptional power and energy at this ratio (4:1:2) could be due to the ordered distribution of the participating constituents. π–π interactions of PA and AB, conjugation of polyaniline chain would have created a strong interfacial connection between their conducting layers and provided a favorable environment for the fast-redox transitions of PA and COF by allowing the ions and electrons through the porous channels (limited amount of COF do not block the channels) [51, 52]. PACOF1 has an outstanding specific power of 2500 W/kg at 20 mA.

The specific power and energy of PACOF1 based system at different current have been provided in Table S4.

Coulombic efficiencies, η of the supercapacitors are calculated from the charging and discharging times obtained from CD plots. PACOF1 took the highest time to get charged and discharged; it also had the maximum value of C_{SP} due to the highest value of discharging time. Other composite based cells took less time than PACOF1 for charging and discharging. So, the Coulombic efficiencies of all the systems were evaluated to study their charge transferability. The following equation is used to estimate the Coulombic efficiency.

$$\eta(\%) = \frac{TD}{TC} \times 100 \qquad (9)$$

T_D represents the discharging time. T_C refers to the charging time.

Table 3 shows that PACOF1 has the maximum coulombic efficiency of 99.1%, and this reflects its excellent effectiveness in terms of charge transfer. Figure 16 demonstrates that the coulombic efficiency of PACOF1 decreases with increase in current.

To find out the practical application of the fabricated supercapacitors, their life spans were evaluated by carrying out 8000 voltammetry cycles at 10 mA (Fig. 17d). PACOF7 (4:4:1) exhibited the minimum drop in the retention of 9.9% after 8000 cycles. AB supplies abundant surface area on which the components settle down, and it also shut out the expected mechanical deterioration of COF and PANI during redox transitions. Similarly, PANI helps in retaining the structural integrity of COF by disallowing any aggregation and volumetric transformation of COF during CV cycles [9, 53]. PACOF6 (4:1:4) showed maximum drop in capacitance retention of 26% after 8000 cycles. An additional amount of cobalt ferrite would have been aggregated in the pores of the microstructures, obstructing the charge transfer and creating more internal resistance [54, 55]. These are probably the primary causes of such a huge drop in retention. PACOF1 (4:1:2) exhibits a satisfactory capacitance retention of 83.5%.

Resistances given by various constituents in the electrochemical configurations were evaluated from electrochemical impedance spectroscopy (EIS). Equivalent series resistance (R_S) is found out from the point of intercept in real axis. R_S is the summation of various resistances like electrolyte impedance,
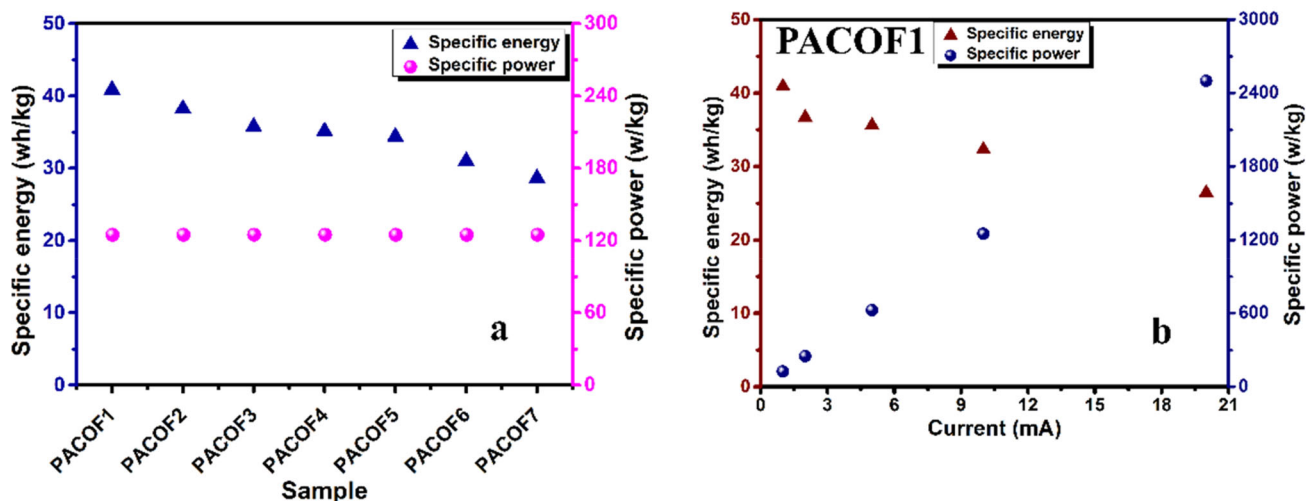
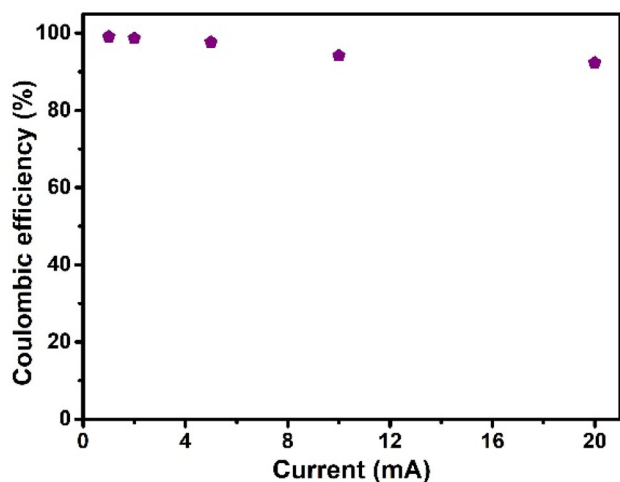Fig. 15 Ragone plot obtained from the two-electrode cell

Fig. 16 Coulombic efficiency of PACOF1 at different current values

electrode-current collector resistance, intrinsic resistance of the materials, and resistance of electrochemically passive components. Charge transfer resistance (R_{CT}) is the diameter of the semicircle in the Nyquist plot at high frequency (Fig. 17a). R_{CT} arises because of a less porous structure or pore blockages and inefficient charge transport [56, 57]. R_S values of all the electrodes have been provided in Table S2 of supplementary file. PACOF3 (4:2:1) has the minimum R_{CT} of 0.5 Ω, and PACOF6 has the maximum R_{CT} of 1.8 Ω. PACOF1 (4:1:2) offers relatively less R_{CT} of 1 Ω. With excess loading of acetylene black, polyaniline and cobalt ferrite particles were scattered and distributed on the surface of AB in an abrupt manner. This would have brought disjointedness in the conducting

networks of the composites resulting in a high R_{CT} [41, 58]. The equivalent electrical circuit for PACOF1 has been given in Fig. 18. Figure 17b demonstrates that the impedance is decreasing with increase in frequency for both higher and lower frequency regions. Figure 17c resembles the the admittance plot of all the prepared electrodes. The knee frequencies have been calculated from the admittance plot (Table S2). It is the maximum value of frequency that predominantly holds the capacitive behavior and reflects the potential of power delivery of a supercapacitor. PACOF1 has the highest knee frequency of 398 Hz; so, it could provide better power response. Figure S3 represents the frequency vs phase angle plot of the systems. It can be seen that the phase angle of all the systems are less than 90°, which represent the pseudocapacitive nature of the composites due to the presence of polyaniline and cobalt ferrite.

4 Conclusion

The current research has been emphasized to evaluate the optimal weight proportion of aniline, cobalt ferrite, acetylene black in the composites considering their electrochemical properties. PACOF1, with the ratio of 4:1:2 (AN:AB:COF), demonstrates the utmost charge containing capacity with 738.65 F/g of specific capacitance. It has the maximum specific energy of 40.9 Wh/kg as well as the highest value of specific power, i.e., 125 W/kg, which makes it the most suitable ratio among all. PACOF1 gives maximum coulombic efficiency of 99.1% due to its remarkable
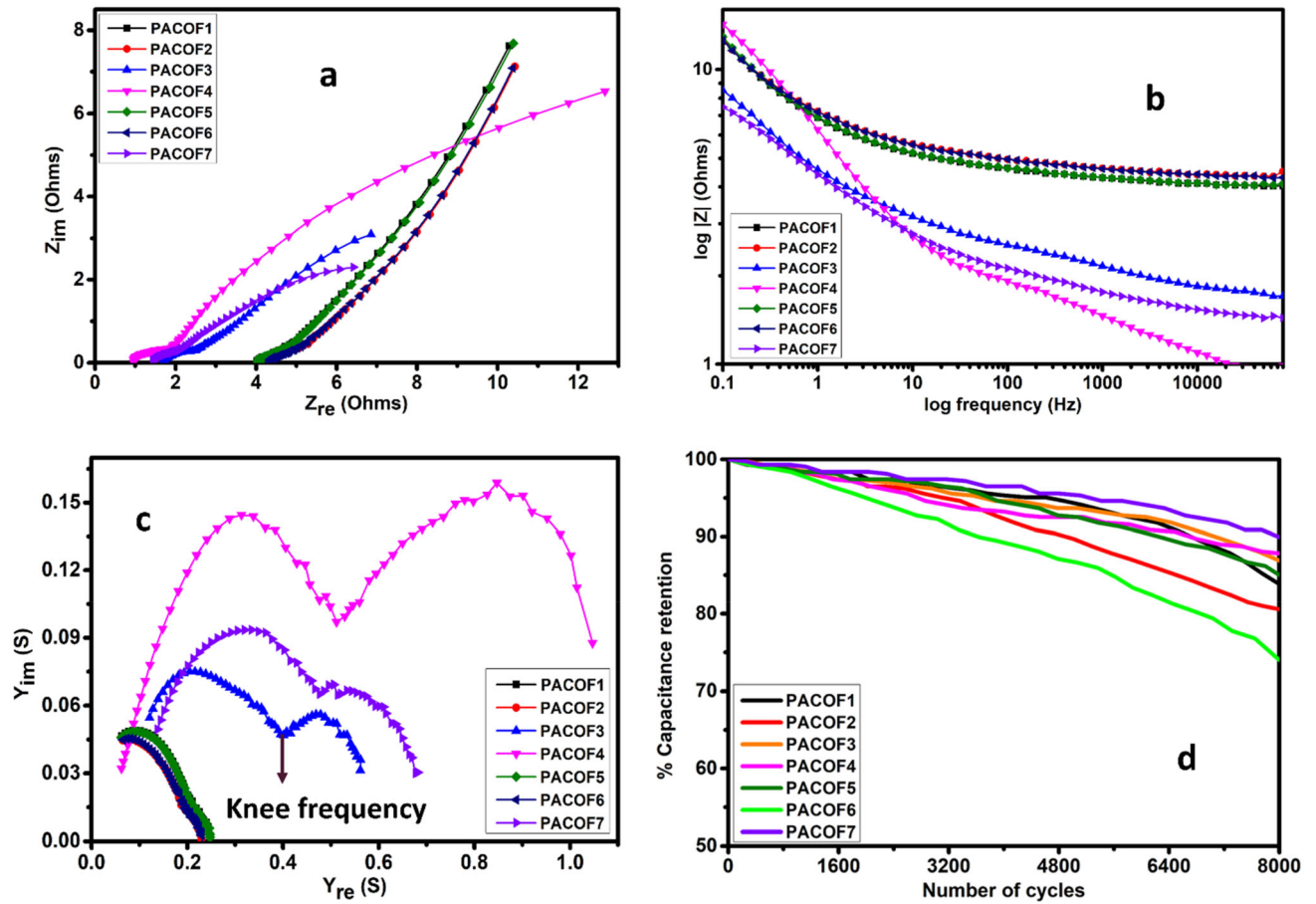
Fig. 17 **a** Impedance plot, **b** frequency vs |Z| plot, **c** admittance plot, **d** cycle life of the fabricated electrodes
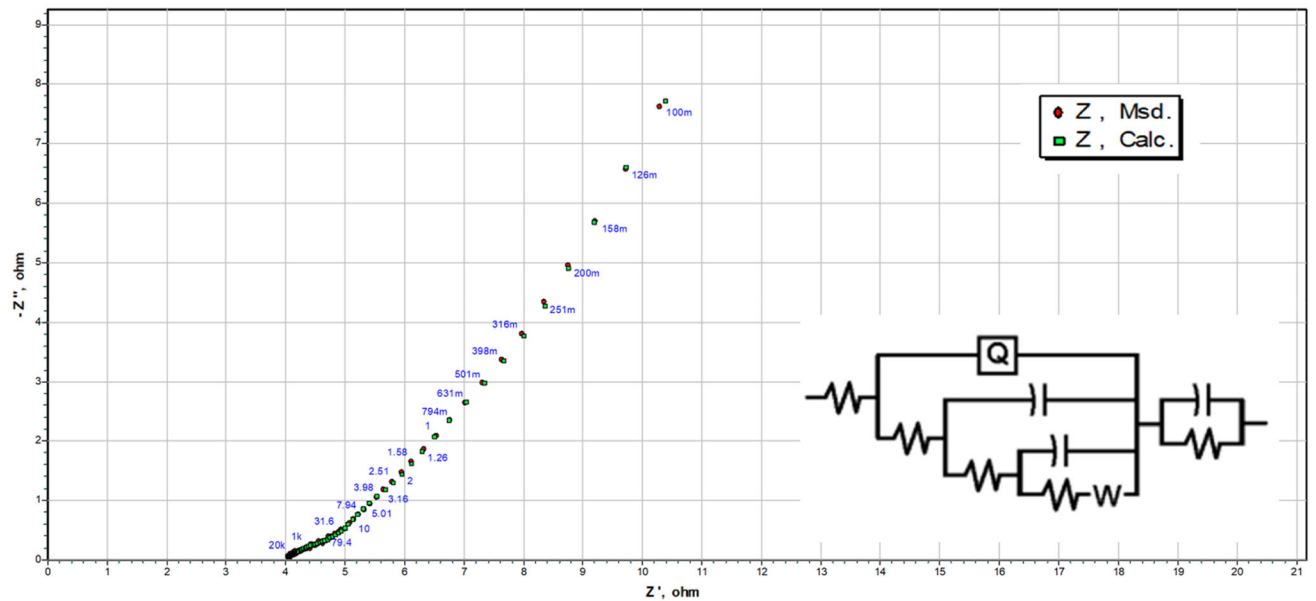

Fig. 18 Equivalent electrical circuit of PACOF1

charge transfer efficiency. After 8000 CV cycles, a fair capacitance retention of 83.5% was found for PACOF1. PACOF1 gives a relatively less charge transfer resistance of 1 Ω. PACOF3, PACOF4, PACOF5 offer lower charge transfer resistances than PACOF1, but PACOF1 provides the highest specific energy, capacitance, specific power. Acetylene black stores charge (ionic) at the interface of electrode and electrolyte by physical adsorption, resulting in excellent electrochemical outcomes like long life span, high discharge speed, charge capacity, and power density. But they offer very less capacitance as they store energy via reversible adsorption. Transition metal oxides and conducting polymers exhibit outstanding energy density and specific capacitance due to the redox transitions at the electrode surface and void spaces available in the composites. Metal oxides offer very poor cycle stability and degraded rate capability because of their dejected intrinsic conductivity. The main aim of acetylene black was to provide adequate surface area to the electrochemically active components (here, COF and PA) and look after the structural integrity of COF and PA by holding out against the mechanical distortion during oxidation–reduction. Initially, the specific capacitance increased with the increase in the amount of AB. This could be due to the uniform distribution of PA and COF without aggregation. After a certain value of AB, the capacitance dropped due to the random distribution of COF and PA. Similarly, when COF crossed a certain value, aggregates would have been formed, resulting in pore blockages and increased internal resistance. Numerous electrochemical properties have been considered to obtain the optimal proportion, and the desired ratio is 4:1:2.

Acknowledgements

Authors contribution

Both the authors have equally contributed to the work.

Data availability

All the required characterization data are available in the supplementary file.

Declarations

References

1. K.V. Sankar, R.K. Selvan, Electrochim. Acta **213**, 469–481 (2016)
2. P. Simon, Y. Gogotsi, B. Dunn, Science **343**, 1210 (2014)
3. M. Winter, R.J. Brodd, Chem. Rev. **104**, 4245 (2004)
4. D.P. Dubal, O. Ayyad, V. Ruiz, P. Gómez-Romero, Chem. Soc. Rev. **44**, 1777 (2015)
5. X. Wu, L. Meng, Q. Wang, W. Zhang, Y. Wang, Mater. Chem. Phys. **206**, 259 (2018)
6. F. Pico, J. Ibañez, M.A. Lillo-Rodenas, A. Linares-Solano, R.M. Rojas, J.M. Amarilla, J.M. Rojo, J. Power Sources **176**, 417 (2008)
7. H. Li, Y. He, V. Pavlinek, Q. Cheng, P. Saha, C. Li, J. Mater. Chem. A **3**, 17165 (2015)
8. S.K. Shinde, D.P. Dubal, G.S. Ghodake, V.J. Fulari, RSC Adv. **5**, 4443 (2015)
9. Q. Meng, K. Cai, Y. Chen, L. Chen, Nano Energy **36**, 268 (2017)
10. R.H. Lee, H.H. Lai, J.J. Wang, R.J. Jeng, J.J. Lin, Thin Solid Films **517**, 500 (2008)
11. Y. Yang, S. Chen, L. Xu, Macromol. Rapid Commun. **32**, 593 (2011)
12. J. Stejskal, D. Hlavatá, P. Holler, M. Trchová, J. Prokeš, I. Sapurina, Polym. Int. **53**, 294 (2004)
13. O.A. Nunoo, J.A. Awuah, E.K.K. Abavare, K. Singh, Int. J. Adv. Res. Eng. Technol. **10**, 157 (2019)
14. A. Torvi, S. Naik, M. Kariduraganavar, Chem. Data Collect. **17–18**, 459 (2018)
15. P. Asen, S. Shahrokhian, A.I. Zad, *Ternary Nanostructures of Cr2O3/Graphene Oxide/Conducting Polymers for Supercapacitor Application* (Elsevier, Amsterdam, 2018)

16. M. Ates, S. Caliskan, E. Ozten, Fuller. Nanotub. Carbon Nanostruct. **26**, 360 (2018)

17. B. Mu, W. Zhang, S. Shao, A. Wang, Phys. Chem. Chem. Phys. **16**, 7872 (2014)

18. K.V. Sankar, R.K. Selvan, J. Power Sources **275**, 399 (2015)

19. A.K. Das, S.K. Karan, B.B. Khatua, Electrochim. Acta **180**, 1 (2015)

20. L. Wang, T. Wu, S. Du, M. Pei, W. Guo, S. Wei, RSC Adv. **6**, 1004 (2016)

21. C. Pan, H. Gu, L. Dong, J. Power Sources **303**, 175 (2016)

22. A.K. Thakur, A.B. Deshmukh, R.B. Choudhary, I. Karbhal, M. Majumder, M.V. Shelke, Mater. Sci. Eng. B **223**, 24 (2017)

23. A. Jeyaranjan, T.S. Sakthivel, C.J. Neal, S. Seal, Carbon **151**, 192 (2019)

24. J. Yang, Y. Yang, J. Lan, Y. Yu, X. Yang, J. Electroanal. Chem. **843**, 22 (2019)

25. P. Haldar, J. Mater. Sci. **31**, 7905 (2020)

26. T. Das, B. Verma, Synth. Met. **251**, 65 (2019)

27. S. Sahoo, S. Zhang, J.J. Shim, Electrochim. Acta **216**, 386 (2016)

28. K.V. Sankar, R.K. Selvan, D. Meyrick, RSC Adv. **5**, 99959 (2015)

29. Sowmya and M. Selvakumar, Int. J. Hydr. Energy **43**, 4067 (2018)

30. S. Chaudhary, A.B.V. Kiran Kumar, N.D. Sharma, M. Gupta, Int. J. Energy Res. **43**, 3446 (2019)

31. D. Zha, P. Xiong, X. Wang, Electrochim. Acta **185**, 218 (2015)

32. L. Shao, Q. Wang, Z. Ma, Z. Ji, X. Wang, D. Song, Y. Liu, N. Wang, J. Power Sources **379**, 350 (2018)

33. L. Yu, M. Gan, L. Ma, H. Huang, H. Hu, Y. Li, Y. Tu, C. Ge, F. Yang, J. Yan, Synth. Met. **198**, 167 (2014)

34. V.S. Jamadade, D.S. Dhawale, C.D. Lokhande, Synth. Met. **160**, 955 (2010)

35. A.G. MacDiarmid, L.S. Yang, W.S. Huang, B.D. Humphrey, Synth. Met. **18**, 393 (1987)

36. P. Saren, A. De Adhikari, S. Khan, G.C. Nayak, J. Solid State Chem. **271**, 282 (2019)

37. K.R. Reddy, B.C. Sin, K.S. Ryu, J. Noh, Y. Lee, Synth. Met. **159**, 1934 (2009)

38. H. Lin, Q. Huang, J. Wang, J. Jiang, F. Liu, Y. Chen, C. Wang, D. Lu, S. Han, Electrochim. Acta **191**, 444 (2016)

39. W. Liu, S. Wang, Q. Wu, L. Huan, X. Zhang, C. Yao, M. Chen, Chem. Eng. Sci. **156**, 178 (2016)

40. Y. Zhao, Y. Xu, J. Zeng, B. Kong, X. Geng, D. Li, X. Gao, K. Liang, L. Xu, J. Lian, S. Huang, J. Qiu, Y. Huang, H. Li, RSC Adv. **7**, 55513 (2017)

41. H. Wang, J. Lin, Z.X. Shen, J. Sci. Adv. Mater. Dev. **1**, 225 (2016)

42. G. Nabi, W. Raza, M.A. Kamran, T. Alharbi, M. Rafique, M.B. Tahir, S. Hussain, N.R. Khalid, Q. ul-Aain, N. Malik, R.S. Ahmed, C.B. Cao, J. Energy Storage **29**, 101452 (2020)

43. P. Xiong, Q. Chen, M. He, X. Sun, X. Wang, J. Mater. Chem. **22**, 17485 (2012)

44. H.L. Girard, H. Wang, A. D'Entremont, L. Pilon, J. Phys. Chem. C **119**, 11349 (2015)

45. P. Zhu, Y. Zhao, Mater. Chem. Phys. **233**, 60 (2019)

46. N. Cai, J. Fu, V. Chan, M. Liu, W. Chen, J. Wang, H. Zeng, F. Yu, J. Alloy. Compd. **782**, 251 (2019)

47. M. Toupin, T. Brousse, D. Bélanger, Chem. Mater. **14**, 3946 (2002)

48. A. Viswanathan, A.N. Shetty, Electrochim. Acta **289**, 204 (2018)

49. M.M. Mezgebe, K. Xu, G. Wei, S. Guang, H. Xu, J. Alloy. Compd. **794**, 634 (2019)

50. Q. Lu, J.G. Chen, J.Q. Xiao, Angew. Chem. Int. Edn. **52**, 1882 (2013)

51. J. Shen, C. Yang, X. Li, G. Wang, ACS Appl. Mater. Interfaces. **5**, 8467 (2013)

52. Z. Yang, A. Qiu, J. Ma, M. Chen, Compos. Sci. Technol. **156**, 231 (2018)

53. M.M. Nobrega, V.L. Martins, R.M. Torresi, M.L.A. Temperini, J. Phys. Chem. C **118**, 4267 (2014)

54. A. Shanmugavani, D. Kalpana, R.K. Selvan, Mater. Res. Bull. **71**, 133 (2015)

55. V.S. Kumbhar, A.D. Jagadale, N.M. Shinde, C.D. Lokhande, Appl. Surf. Sci. **259**, 39 (2012)

56. Q. Zhang, N. Wang, P. Zhao, M. Yao, W. Hu, Compos. A **98**, 58 (2017)

57. L.M. da Silva, D.A. de Lima Almeida, S.S. Oishi, A.B. Couto, N.G. Ferreira, Mater. Sci. Eng. B **228**, 249 (2018)

58. G. Wang, L. Zhang, J. Zhang, Chem. Soc. Rev. **41**, 797 (2012)

Springer